Gold nanoparticle/MXene for multiple and sensitive detection of oncomiRs based on synergetic signal amplification

Mohammadniaei, Mohsen; Koyappayil, Aneesh; Sun, Yi; Min, Junhong; Lee, Min-Ho

Published in:
Biosensors and Bioelectronics

Link to article, DOI:
10.1016/j.bios.2020.112208

Publication date:
2020

Document Version
Peer reviewed version

Gold Nanoparticle/MXene for Multiple and Sensitive Detection of OncomiRs based on Synergetic Signal Amplification

Mohsen Mohammadniaei[a,b], Aneesh Koyappayil[a], Yi Sun[b], Junhong Min[a,*], Min-Ho Lee[a,*]

[a] School of Integrative Engineering, Chung-Ang University, Heukseok-dong, Dongjak-gu, Seoul 06910, Republic of Korea.

[b] Department of Health Technology, Technical University of Denmark, Kongens Lyngby, DK-2800, Denmark.

*** Correspondence:** mhlee7@cau.ac.kr (M.-H. L.); junmin@cau.ac.kr (J. M.);

Tel.: +82-2-820-5503 (M.-H.L.); +82-2-820-5348 (J.M.); Fax: +82-2-814-2651 (J. M. & M.-H. L.).

Abstract

Multiple and sensitive detection of oncomiRs for accurate cancer diagnostics is still a challenge. Here, a synergetic amplification strategy was introduced by combining a MXene-based electrochemical signal amplification and a duplex-specific nuclease (DSN)-based amplification system for rapid, attomolar and concurrent quantification of multiple microRNAs on a single platform in total plasma. Synthesized MXene-$Ti_3C_2T_x$ modified with 5 nm gold nanoparticles (AuNPs) was casted on a dual screen-printed gold electrode to host vast numbers of DNA probes identically co-immobilized on dedicated electrodes. Interestingly, presence of MXene provided biofouling resistance and enhanced the electrochemical signals by almost 4 folds of magnitude, attributed to its specious surface area and remarkable charge mobility. The 5 nm AuNPs were perfectly distributed within the whole flaky architect of the MXene to give rise to the electrochemical performance of MXene and provide the Thiol-Au bonding feature. This synergetic strategy reduced the DSN-based biosensors´ assay time to 80 min, provided multiplexability, antifouling activity, substantial sensitivity and specificity (single mutation recognition). The limit of detection of the proposed biosensor for microRNA-21 and microRNA-141 was respectively 204 aM and 138 aM with a wide linear range from 500 aM to 50 nM. As a proof of concept, this newly-developed strategy was coupled with a 96-well adaptive sensing device to successfully profile three cancer plasma samples based on their altered oncomiR abundances.

Keywords: microRNA, multiple detection, electrochemical, biosensor, duplex specific nuclease, MXene

1. Introduction

Early clinical diagnosis of cancer is crucial to improve the treatment outcomes and understand the disease development process. Current cancer diagnostics mainly rely on single or non-specific biomarker detection which does not provide sufficient information for the clinicians in diagnosis and prognosis (Wu and Qu 2015). As the very potent clinical biomarkers for the early cancer diagnostics, microRNAs (miRNAs) have received intensive attentions from biomedical researchers and clinicians due to their distinct expression levels in various cancer types through different development stages (Mohammadniaei et al. 2017). Compared to the other biomarkers, miRNAs can be easily obtained *via* liquid biopsy from bodily fluids such as urine, blood, tears, saliva, breast milk, etc. They have also the advantages of high specificity, robustness at room temperature (RT), facile and low cost detection routes, non-invasiveness, and more importantly, being used as the multiple biomarkers simply by designing the corresponding complementary nucleic acid probes without any restrictions (Wang et al., 2016). Whereas, protein biomarker detection usually involves the usage of antibodies, which imposes cost to the system; also in many cases, antibodies are not commercially available and their synthesis procedure is highly skill-oriented and time-consuming (Condrat et al., 2020).

However, miRNA quantification in real samples is challenging, due to their very homologous sequences and low abundance in bodily fluids (ranging from fM to nM) (Mohammadi et al., 2018; Kilic et al., 2018). Knowing that, only a few percentage of total plasma RNA (6 to 300 ng/mL) is accounted for miRNAs (Weber et al., 2010), development of a very sensitive biosensor for multiple detection of miRNAs is highly demanding to precisely screen diverse cancer types at their early stage of developments.

Standard analytical methods have been employed for miRNA quantification such as quantitative real-time polymerase chain reaction (qRT-PCR), northern blotting and microarrays (Kilic et al. 2018). However, complicated systems for short nucleic acid analysis together with high operation costs have hampered their applications in the miRNA field. Besides, electrochemical biosensors have offered more desirable platforms for multiple detection of miRNAs due to their high degree of sensitivity, low cost and simplicity (Maduraiveeran et al. 2018; Mohammadniaei et al. 2019c). DNA tetrahedral scaffold (Chen et al. 2018a), hybridization chain reaction and Y-shaped DNA (Zhou et al., 2019; Guo et al., 2019) have demonstrated very good performances for sensitive miRNA detection, yet they are limited to one target detection and complex nucleic acid design. Lately, electrochemiluminescence and photoelectrochemical detection of miRNA have represented ultra-sensitivity and promising performances. Although, they are not multiplex and are still hampered by either complicated probe design or several detection steps (Zhang et al., 2019; Wang et al., 2019).

Towards multiplexing, quantum dot barcode-coupled ligase chain reaction was introduced for multiple miRNA detection. The assay time was significantly short (< 70 min), however, it suffered from narrow dynamic range as well as difficulty in identical co-immobilization of two capture probes on a single magnetic bead (Zhu et al. 2014). Femtomolar quantification of miR-21 and miR-141 was also reported using the combination of electrochemiluminescence and electrochemical methods (Feng et al. 2016). Although, besides the laborious fabrication of nanostructures, using one redox label hindered simultaneous measurement of both targets at the same time. Recently, a generic neutravidin-based electrochemical biosensor was fabricated for synchronized quantification of miR-21 and miR-141 with the advantages of simplicity and low cost. Yet the developed biosensor represented a low sensitivity, also the competitive conjugation of nanolabels on the neutravidins would result in measurement errors (Azzouzi et al. 2019).

Enhancing the sensitivity and performance of electrochemical biosensors can be achieved *via* engagement with nanomaterials and integration with signal amplification techniques such as duplex-specific nuclease (DSN) amplification .Though, despite their simplicity of primer design, high specificity toward single mutations and low contamination risks, current DSN-based biosensors are mainly designed for one target detection and/ or their whole assay times take usually more than 2 h to hamper their clinical translations (Lu et al. 2019; Wang et al. 2018; Xiao et al. 2019). Therefore, introducing a new material and a novel strategy would be an alternative to alleviate those challenges. More details of the previous reports are provided in Table S1.

MXenes as the newly-emerged class of 2D materials have gained growing interests in biomedical and biosensing applications due to their unique physiochemical features (Mohammadniaei et al. 2019b; Zhu et al. 2017). These layered structures possess the general chemical formula of $M_{n+1}X_nT_x$, from which M refers to a transition metal atom, n = 1, 2, or 3, X symbolizes C and/or N atoms, and T_x indicates the surface groups (e.g. F, O, Cl, OH). Within various types of MXenes, the $Ti_3C_2T_x$ has shown more significant properties for electrochemical applications (Kumar et al. 2018; Lorencova et al. 2017). The accordion-like nanoflake architecture and surface group richness of MXene-$Ti_3C_2T_x$ provide a very spacious surface for enzyme/nucleic acid loading and further target detection. In addition, its biocompatibility, high charge mobility and electrocatalytic activity together with its ability to passivate the biofouling effects have made this material a perfect model for the applications in electrochemical biosensors (Liu et al. 2019). Recently, gold nanoparticle (AuNP) decoration of MXene has reported to enhance the electrocatalytic activity of MXene, however, the reported methods have a serious issue as they are based on the chemical reduction of $HAuCl_4$ (Li et al. 2018; Rakhi et al. 2016). Since, the standard potential (E^o) of Au and Ti atoms are respectively +1.52 V and -1.37 V, spontaneous oxidation of

Ti (in $Ti_3C_2T_x$) *via* Au^{3+} (in $HAuCl_4$ solution) is inevitable to demolish the chemical structure and physiochemical properties of MXene-$Ti_3C_2T_x$.

We have recently developed very sensitive miRNA biosensors (Lee et al. 2020; Mohammadniaei et al. 2019a), however to reduce the assay time, simplify the primer design and supply multiple detection aptitude, in this work, we combined DSN and electrochemical signal amplification techniques for rapid (80 min) and multiplex detection of miR-21 and miR-141 on a single electrode in attomolar level. The rationale behind choosing those target miRNAs was to perform a better cancer screening, since they are well-known cancer biomarkers and have distinctive and comparable expression levels in our studied cancer plasma samples (lung, breast and prostate cancers) (Abd-El-Fattah et al., 2013; Guo et al., 2015; Li et al., 2017; Liu et al., 2017; Mishra et al., 2014; Song et al., 2010).

For the DSN amplification, using a novel strategy, two magnetic particles (MPs) were functionalized with two different single-stranded DNAs (ssDNAs) labeled with methylene blue (MB) and ferrocene (Fc), which were partially complementary to the target miRNAs, correspondingly (Fig. 1). After the invasion of targets and amplification cycle, the released uncleaved DNA sequences harboring redox labels were hybridized with the electrochemical sensor platforms for subsequent measurements. For the electrochemical signal amplification, a home-made screen printed gold electrode (SPGE) was modified with the synthesized $Ti_3C_2T_x$ and decorated with 5 nm AuNP (AuNP@MXene/Au) and further loaded with abundant ssDNAs (Base) to provide a significantly higher electrochemical signal than that of the AuNP/Au electrodes (c.a. 4 times). Using a simple experiment, for the first time we could calculate distinctive contributions of charge mobility and surface area of MXene-$Ti_3C_2T_x$ on the electrochemical signal enhancement. Despite the multiple detection, high specificity and great potential of the fabricated device for point

of care (POC) cancer screening, our developed system could resist against biofouling and non-specific bindings and was able to operate in real sample matrices to successfully screen different cancer plasma samples.

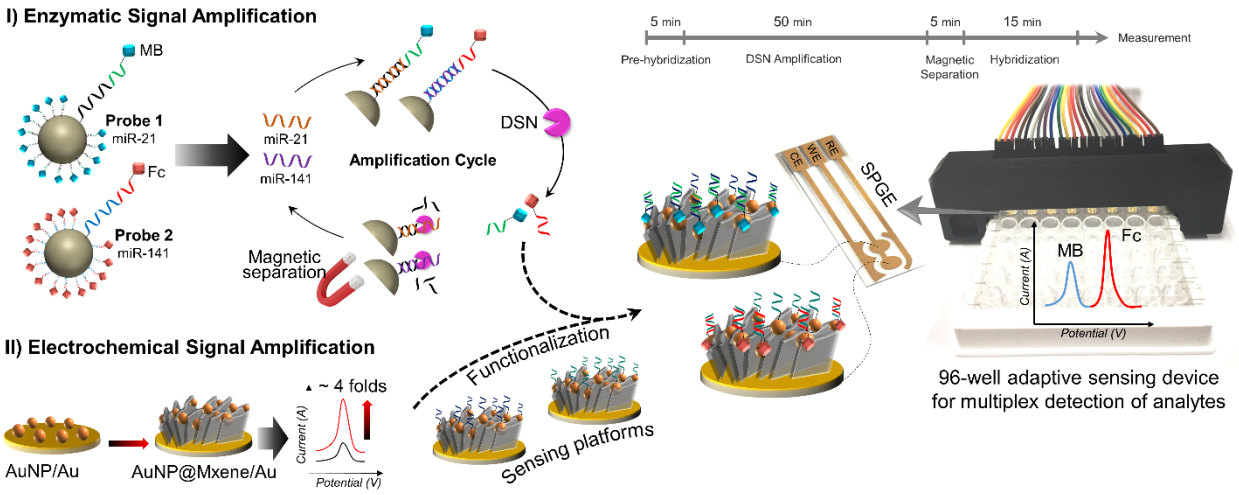

Figure 1. Schematic diagram representing the whole assay procedure for multiplex detection of miR-21 and miR-141.

2. Materials and methods

2.1. Materials and reagents

Screen printed gold electrodes (SPGEs) with two active sites of 2.0096 mm^2 as well as the sensor connector were designed by the authors and purchased from National NanoFab Center (ROK), Korea. (3-mercaptopropyl)trimethoxysilane (MPTMS), 6-Mercapto-1-hexanol (MCH), hydrofluoric acid (HF; ACS reagent, 48 %), ethanol, Nafion® 10 wt. % dispersion in water, Tris (2-carboxyethyl) phosphine hydrochloride (TCEP), Tris-HCl, $MgCl_2$, ferrocenecarboxylic acid, sodium chloride (NaCl), potassium chloride (KCl), ethylenediaminetetraacetic acid (EDTA), 4-(2-hydroxyethyl)-1-piperazineethanesulfonic acid (HEPES buffer; pH 7.4), Tween™ 20, bovine Serum Albumin (BSA), human serum albumin (HSA), potassium hexacyanoferrate (II) trihydrate, N-(3-dimethylaminopropyl)-N′-ethylcarbodiimide hydrochloride (NHS), N-(3-

Dimethylaminopropyl)-N′-ethylcarbodiimide hydrochloride (EDC), urea, potassium ferricyanide, potassium ferrocyanide, 2-(N-Morpholino)ethanesulfonic acid (MES), hexaammineruthenium (iii) chloride, chloroform and isopropanol were purchased from Sigma-Aldrich (USA). Titanium aluminium carbide powder (Ti_3AlC_2; 99.9 %) was purchased from Shanghai Xinglu Chemical Technology Co. RNase-free phosphate buffered saline (PBS) (10X) pH 7.4, ultrapure™ DNase / RNase-free distilled water (NFW), (3-((3-cholamidopropyl) dimethylammonio)-1-propanesulfonate) (CHAPS) and TRIzol™ were purchased from ThermoFisher Scientific. 5 nm and 30 nm colloidal AuNPs were purchased from BBI Solutions (UK). All of the oligonucleotides were obtained from Bioneer® (Korea) and subsequently dissolved in DEPC-treated H_2O. The oligonucleotide sequences are provided in Table S2.

2.2. Analytical instruments

For MXene-$Ti_3C_2T_x$ characterization, X-ray powder diffraction (XRD) was recorded using a Bruker-AXS New D8-Advance X-ray diffractometer. Also, X-ray photoelectron spectroscopy (XPS) was performed by means of K-alpha$^+$ X-ray photoelectron spectroscope (ThermoFisher Scientific), and the spectra deconvolution was done using XPSPEAK 41 software. For evaluation of the surface morphology of electrodes, Carl Zeiss SIGMA field emission scanning electron microscope (FE-SEM) was used which was equipped with X-ray energy-dispersive spectrometry (EDS) for elemental composition analysis of electrodes under 20.0 kV Acc. voltage. Distilled and deionized (DI) water (resistance ≥ 18 MΩ) was produced using Milli-Q® System (Millipore Corp.). For magnetic particle (MP)/nucleic acid conjugation test as well as the DSN activity evaluation, UV–Vis spectrophotometer (Jasco V530; Easton, MD, USA) and NanoDrop ND-1000 (DE, USA) were used.

All the electrochemical analysis were carried out using an IVIUM electrochemical workstation (CompactStat.h, Ivium Technologies B.V.). Cyclic voltammetry (CV) was carried out at a scan rate of 50 mV/s in HEPES (pH 7.4) with the potential window of −0.5 V to +0.8 V and −0.35 V to −0.1 V; also in PBS (pH 7.4) containing 5 mM $Fe(CN)_6^{4-/3-}$ and 0.1 M KCl with the potential window of 0.0 V to +0.5 V. Differential pulse voltammetry (DPV) was conducted over a potential window of −0.5 to +0.5 V at a scan rate of 50 mV/s with 80 mV pulse amplitude and 30 ms pulse time. Chronocoulometry was conducted in 20 mM KCL and hexaammineruthenium(iii) chloride (200 µM) + KCl (20 mM) with 0.5 s pulse width, 0.00025 s sample interval as well as initial and final potentials of −0.1 and +0.1 V, respectively. Electrochemical impedance spectroscopy (EIS) experiment was performed at open circuit potential (equilibrium potential) within the frequency range of 0.1 Hz to 1 MHz with the applied AC voltage of 5 mV. The recorded impedance spectra were fitted on the proper equivalent circuits using an interface on the IVIUM software.

2.3. Synthesis of MXene-$Ti_3C_2T_x$

MXene-$Ti_3C_2T_x$ was synthesized by aluminum etching from Ti_3AlC_2 MAX phase in HF at RT. Briefly, Ti_3AlC_2 MAX phase (5.0 g) was dissolved in 50 mL HF (48 %) under constant stirring for 24 h to form a homogeneous suspension. The obtained suspension was rinsed with DI water several times until it reached pH ≥ 6. After gentle sonication (1 h), centrifugation and decantation, the suspension was washed with ethanol (99.9 %) and allowed to dry at RT for 2 days. The resulting MXene-$Ti_3C_2T_x$ was stored at 4 ºC for further experiments.

2.4. Modification of SPGE with MXene and gold nanoparticles (AuNP@MXene/Au)

Prior to modification, bare SPGEs were washed sequentially with DI water and ethanol, then subjected to oxygen plasma to produce hydrophilic surfaces, selectively on the working areas. SPGEs were further cleaned using electrochemical etching by conducting CV technique for several scans from -0.5 V to 1.2 V in 0.5 M H_2SO_4 until reaching stable voltammograms (Fig. S1). Electrodes were then washed with DI water and NFW before drying under a stream of nitrogen.

The synthesized MXene was dissolved in DI water (0.1 mg/mL) containing 0.1% Nafion and sonicated for 60 min at RT. Next, 4 µL of the suspension was drop-casted on the working electrodes and allowed to dry at RT. The electrodes were then immersed in 1 mM MPTMS (dissolved in ethanol) for 2 h at RT. Later, the electrodes were washed and treated with 4 µL of 5.00×10^{13} AuNPs (5 nm) for 2 h at 4 ºC in a humid chamber. After gentle washing with NFW and drying under nitrogen, the modified electrodes (AuNP@MXene/Au) were stored at 4 ºC for further characterization and measurement.

2.5. MP functionalization with DNA probes

For the assembly of DNA probes (DNA^{141} and DNA^{21}) on the streptavidin-coupled MPs (Dynabeads™ M-280 Streptavidin; ThermoFisher Scientific, USA), we used oligonucleotides which were biotinylated at their 3′-end and labeled with MB or Fc or 6-carboxyfluorescein (FAM) at their 5′-end. 300 µL of MPs (10 mg/mL) were washed twice with Tris buffer and resuspended in the same buffer. Next, the MPs were incubated with 100 µL of 10 µM biotinylated DNAs (dissolved in NFW or TE buffer) with gentle shaking at RT for 30 min. After that, the functionalized particles were washed twice with 300 µL of Tris-HCl buffer (50 mM; pH 7.4) containing 0.01%

[v/v] Tween™ 20 and 0.01% [w/v] BSA, followed by storage in the Tris-HCl buffer (50 mM; pH 7.4) at 4 ºC.

2.6. Fabrication of sensor platforms

Sensor platforms were fabricated by immobilization of the thiolated ssDNAs ($Base^{21}$ and $Base^{141}$) on each one of the working electrodes, correspondingly. 10 µM of $Base^{21}$ and $Base^{141}$ dissolved in the Tris-HCl buffer (50 mM; pH 7.4) were treated with TCEP (0.1 mM) for 90 min at RT. After desaltation using Zeba spin desalting columns, 7K MWCO, 0.5 mL (ThermoFisher Scientific), 4 µL of $Base^{21}$ and $Base^{141}$ were immobilized onto AuNP@MXene/Au in the presence of 10 mM $MgCl_2$, correspondingly. After 2 h of incubation at RT followed by overnight storage at 4 ºC in a humid chamber, the electrodes were washed thoroughly with NFW and immersed in MCH solution (0.1 mM in ethanol) for 15 min to eliminate physical adsorptions. Later, electrodes were washed with ethanol and NFW, dried with nitrogen and stored in a proper humid chamber at 4 ºC for further use.

2.7. Activity of DSN enzyme on miRNA:DNA heteroduplexes

Activity of DSN on miRNA-DNA duplex was adjusted through the optimization of reaction conditions including concentrations of DSN, reaction temperature and time. A dual-modified DNA probe harboring biotin at its 3′-end and FAM at its 5′-end was assembled on the MP surface according to the protocol provided in section 2.5. The whole DSN cleavage assay was based on the total sample volume of 100 µL. For the optimization of reaction temperature, 5 µL miR^{21} (10 µM; dissolved in Tris buffer), 1 µL DSN (0.5 U/µL), 2.5 µL RNase inhibitor (20 U/µL), 5 µL $MgCl_2$ (200 mM) and 86.5 µL MP-DNA^{21}/FAM conjugate were mixed and incubated at various

temperatures of 40, 45, 50, 55, 60, 65 and 70 ºC for 60 min following by 5 min magnetic separation. The supernatant (90 µL) was then extracted and transferred to a Corning® 96 well half-area black microplate (Sigma Aldrich) for fluorescence measurement of FAM at 520 nm. For the optimization of DSN enzyme concentration, similar protocol was followed, however, here the temperature was fixed at the optimum 60 ºC and the DSN concentration varied from 0 to 1 U/µL. Likewise for the optimization of reaction time, 5 µL miR^{141} (5 nM, 50 nM and 500 nM), 1 µL DSN (optimum 0.8 U/µL), 2.5 µL RNase inhibitor (20 U/µL), 5 µL $MgCl_2$ (200 mM) and 86.5 µL MP-DNA^{141}/Fc conjugate were mixed and incubated at 60 ºC. The reaction was stopped at different incubation times (with the interval of 10 min) followed by 5 min EDTA (final concentration: 10 mM) treatment at RT, 5 min magnetic separation at RT and 15 min hybridization of supernatant (10 µL) with $Base^{141}$/AuNP@MXene/Au in the presence of 100 mM NaCl. After washing the electrodes, oxidation peak current arising from Fc was monitored for each time points.

2.8. Hybridization of DSN amplification products with sensing platforms

After DSN amplification for 50 min, EDTA at the final concentration of 10 mM was added to the reaction mixture with incubation for 5 min to chelate Mg^{2+} and stop the DSN activity. Under magnetic field, 10 µL of the supernatant was mixed with 1 µL NaCl (1 M) and dropped on the sensing platforms with incubation at RT for 15 min. Subsequently, the electrodes were washed thoroughly with HEPES buffer and inserted in the sensor multi-connector. The multi-connector was installed on 96-well plate containing 200 µL HEPES buffer (pH 7.4) for electrochemical measurements.

2.9. Spike-in miRNA sample preparation

For the serum sample denaturation and protection of endogenous miRNAs from nucleases, according to our previously-reported protocol (Mohammadniaei et al. 2019), after centrifugation of HSA for 10 min (14,000 rpm; RT), 10 volume of the cell-free supernatant was mixed with 100 volume of TRIzol^{TM} containing an excess amount of tRNA and 1 volume of QIAGEN proteinase K, followed by incubation at RT for 20 min. Later, various concentrations of synthetic miR-21 and miR-141 were spiked in the prepared serum and vortexed immediately. It should be noted that, in order to avoid degradation of the spike-in miRNAs by the serum nuclease, it is important to add the synthetic miRNAs in this step. Later, CHAPS at the final concentration of 10 μM was added to the solution and mixed with pipetting. Subsequently, for the organic/aqueous separation, 0.2 volumes of molecular grade chloroform was added to the solution following by vortexing for 30 s and centrifugation for 15 min (12,000 rpm; RT). The clear liquid at the top of the mixture (aqueous phase containing nucleic acids) was carefully extracted for further analysis.

2.10. Isolation of miRNA from plasma

Prior to the experiment, plasma samples were incubated on ice for several minutes following by gentle mixing by inverting. For miRNA isolation from plasma, QIAamp® Circulating Nucleic Acid kit was used according to our previous modified protocol (Mohammadniaei et al. 2019). Briefly, plasma (200 μL) was firstly mixed with QIAGEN proteinase K (26 μL) with incubation at RT for 30 min to inactivate the nuclease. Next, ACL buffer containing an excess amount of tRNA (220 μL) together with ATL buffer (66 μL) were added to the mixture following by incubation for 30 min at 60 ºC to release nucleic acids from their inclusions. Subsequently, ACB buffer (600 μL) and isopropanol (460 μL) and CHAPS (10 μM) were mixed with the lysate and incubated on ice

for 5 min. Finally, using QIAamp mini column, the resulting solution was washed and eluted according to the manufacturer protocol.

3. Results and discussion

3.1. Characterization of AuNP@MXene/Au electrode

Morphological structure of the as-prepared MXene-$Ti_3C_2T_x$ and AuNP@MXene/Au electrode were analyzed using FE-SEM. As seen in Fig. 2a, the layered accordion-like architecture of MXene is evidential having thin and transparent nanoflakes stacked on each other. Fig. 2b and c show the SEM images of the AuNP@MXene/Au. High abundance of 5 nm AuNPs are well-distributed on the surface and in between the layers of the MXene (refer to Fig. S2 for control experiment), possibly because of the small size of AuNPs (5 nm) to facilitate the physical diffusions. From the observed image, which was obtained after the sequential washing of electrodes, the high binding efficiency between AuNPs and MXene can be perceived that might be due to the high surface-to-volume ratio of 5 nm AuNPs. The supplementary EDS, XRD and XPS survey spectra, showing the elemental composition analysis of MXene, are provided in supporting information S.1 and Fig. S3.

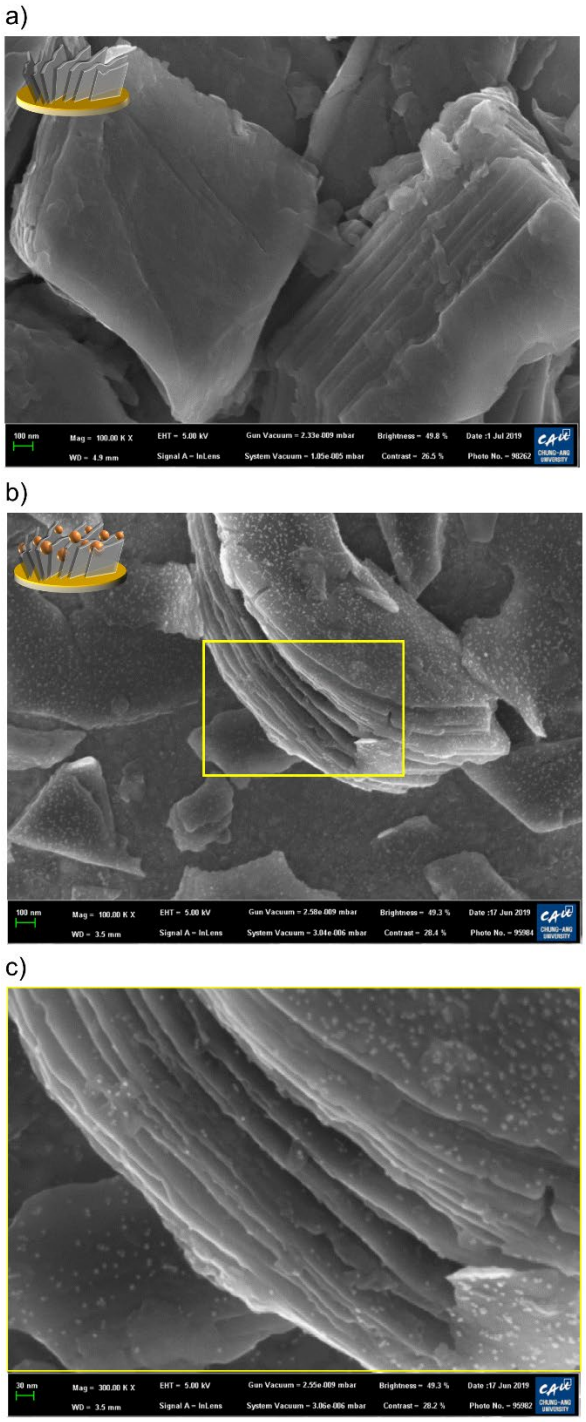

Figure 2. FE-SEM images of: a) As-synthesized MXene-$Ti_3C_2T_x$, b) AuNP@MXene, and c) Magnified image from the boxed region in (b); White dots represent the 5 nm AuNPs.

3.2. Function of MXene on electrochemical activity of the modified electrodes

Electrochemical activity of the modified electrodes was studied using CV, EIS and DPV techniques. In order to investigate the role of MXene on the electrochemical activity of AuNP@MXene/Au electrode, we prepared another type of electrode by modification of Au electrode only with AuNP (AuNP/Au). Both types of electrodes were directed to EIS and CV measurement in PBS. From the Nyquist plots recorded for the two types of electrodes (Fig. 3a), charge transfer resistance value (R_{ct}) of AuNP/Au was measured 623.2 Ω, while it was considerably lower for AuNP@MXene/Au electrode (165.1 Ω) to illustrate its higher electron conductivity resulting from the presence of MXene. Likewise, the corresponding cyclic voltammograms in the Fig. 3a (inset) show the higher electrochemical redox peaks of the AuNP@MXene/Au compared with the AuNP/Au.

We quantified the surface density of DNA immobilized on the AuNP@MXene/Au and AuNP/Au electrodes according to the previously reported method (Steel et al. 1998). Both types of electrodes were treated with an excess amount of thiolated ssDNA (Base^{141}; 20 μM) in order to ensure the maximum surface coverage of ssDNAs. After the electrode backfilling, the cationic redox molecule ruthenium hexaammine (RuHex) was electrostatically bound to the DNA backbones and the surface density of DNA was calculated based on double-layer charge determination (for the calculation details refer to supporting information S.2). As seen in Fig. 3b, there is a significant difference between the recorded charge for DNA-modified AuNP@MXene/Au and AuNP/Au, such that, the surface density of DNA on AuNP@MXene/Au was calculated 3.76×10^{13} molecule/cm^2, being 3.45 folds of magnitude greater than that of the AuNP/Au (1.09×10^{13}).

To calculate the exact value of the enhanced electrochemical signal, both types of electrodes, which were densely modified with $Base^{141}$, were hybridized with complementary Fc-labeled DNA strands (refer to supporting information S.3 and Fig. S4) and directed to DPV measurement. As seen in Fig. 3c (top graph), compared with the AuNP/Au, AuNP@MXene/Au exhibited a pronounce increase in the Fc oxidation peak current by 4.05 times of magnitude. This amplified signal might be resulted from two factors of (i) surface area enhancement, due to the 3D and layered structure of MXene and (ii) charge mobility increment, because of the high electrocatalytic activity of MXene. Therefore, we conducted a simple experiment to clarify the role of each compartments on the observed signal amplification. Very less amount of $Base^{141}$ (1 pM $\approx 3 \times 10^6$ molecule / 5 μL) was immobilized on both electrode types, in order to make sure that equal numbers of molecules were conjugated to the both surfaces. As a result, the role of surface area enhancement would not affect the possible signal increment. As seen in Fig. 3c (bottom graph), interestingly, the Fc oxidation peak current for AuNP@MXene/Au was about 1.48 times higher than the AuNP/Au to illustrate the role of MXene on the charge mobility enhancement of the modified electrode. As a result, as demonstrated in Fig. 4d, 15.7% of the enhanced signal might be attributed to the charge mobility enhancement, while the rest can be assigned to the surface area expansion which was about 3.57 times greater than AuNP/Au. The acquired result was quite interesting, as the magnitude of the surface coverage calculated by DPV was somewhat similar to the value obtained in Fig. 3b, even though we had speculated that the calculation of DNA surface coverage based on the method provided by Steel et al. would consider the charge mobility term as well.

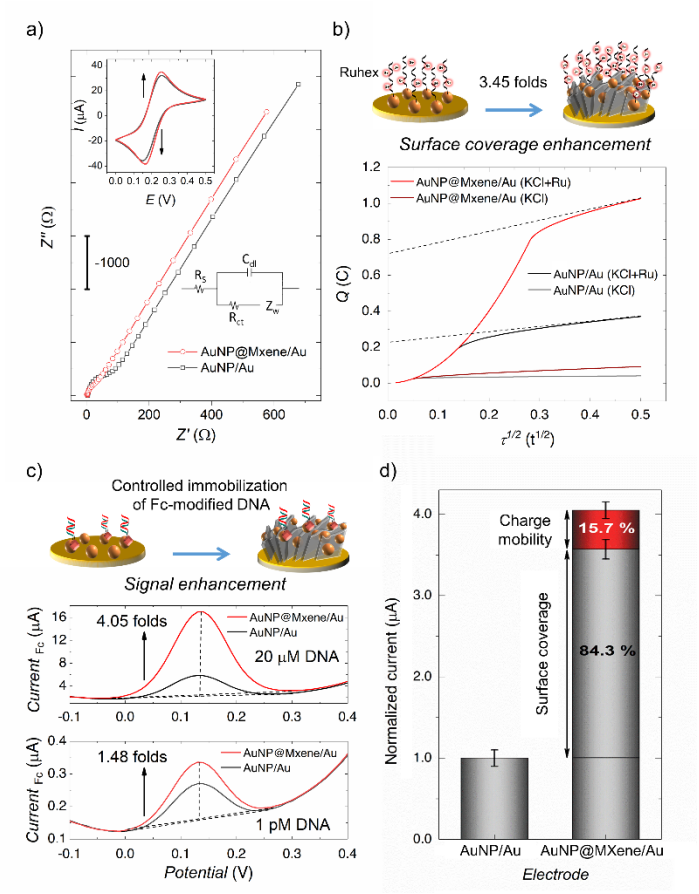

Figure 3. a) Nyquist plots (Z′ vs.− Z″) obtained for AuNP/Au and AuNP@MXene/Au and the equivalent Randles circuit model; Inset shows the corresponding cyclic voltammograms of AuNP/Au (black) and AuNP@MXene/Au (red); Experiments were performed in PBS (pH 7.4) comprising 5 mM of Fe $(CN)_6$ $^{4-/3-}$ and 0.1 M KCl with CV scan rate of 50 mV/s;. b) Typical chronocoulometric response of RuHex on AuNP/Au and AuNP@MXene/Au in 20 mM KCL and hexaammineruthenium(iii) chloride (200 µM) + KCl (20 mM); Dash lines show the outward stretching tangents extrapolated to the Y-axis illustrating the intercept values. c) DPV curves obtained for Base^{141}/AuNP/Au and Base^{141}/AuNP@MXene/Au after being hybridized with uncleaved Fc-labeled DNA sequences (DSN products of 20 µM and 1 pM miR-141 reaction). d) Statistical analysis of the normalized oxidation current peak value of Fc obtained from Fig. 3c.

3.3. Multiplex detection of miR-141 and miR-21

To attain a superior sensing performance, DSN activity was firstly optimized. Using MP functionalized with FAM-labeled DNA (MP-DNA^{21}/FAM) which was complementary to miR-21

(refer to Table S2 for oligonucleotide sequences), the reaction temperature, time and the DSN concentration were optimized to 60 ºC, 0.8 U/µL and 50 min, respectively (refer to supporting information S.4 anf Fig. S5). Then, versatility of the proposed sensing device for multiplex and simultaneous quantification of miR-21 and miR-141 was investigated. The two target miRNAs (5 µL each) were serially diluted in Tris buffer from 500 nM to 50 aM and subjected to DSN-assisted target recycling following by electrochemical measurement of the uncleaved labeled DNA sequences (DSN products). As the sensor response, the DPV curves for different concentrations of target miRNAs are shown in Fig. 4a. Two discrete current peaks can be clearly seen resulting from the oxidation of MB (c.a. −0.26 V) and Fc (c.a. +0.14 V) which were respectively attributed to the detection of miR-21 and miR-141. As depicted, the current peaks of MB and Fc gradually increased with increasing the concentrations of miR-21 and miR-141 from 500 aM to 50 nM, resulting from hybridization of more DSN products to the corresponding sensing platforms. The significant linear performance of the developed biosensor towards serial concentrations of both miRNAs from 500 aM to 50 nM can be evidently seen in Fig. 4b and c. Although, higher concentrations of target miRNAs did not show a considerable change in the oxidation peak currents due to the saturation of sensing platforms. The limit of detection (LOD) for miR-21 and miR-141 were respectively calculated 204 aM and 138 aM. The significant accuracy of our developed sensing device can be comprehended from Fig. S6, as it shows the raw DPV data recorded from 8 electrodes set detecting serial concentrations of target analytes, which is due to the controlled and identical co-immobilization of $Base^{21}$ and $Base^{141}$ on the AuNP@MXene/Au electrodes.

In order to show the high precision and reliability of the fabricated device, concentration of one analyte was maintained constant while the other analyte varied from 500 am to 50 nM. As shown in Fig. 4d-g, the sensor represented linear response toward varied miRNA levels, whereas no significant change was seen for the fixed miRNAs to demonstrate the very negligible

interference between MB and Fc labels (for more details refer to supporting information S.5 and Fig. S7). Moreover comparing the regressions, almost identical equations were seen from the sensor performance for single and multi-detection, indicating the excellent performance of the developed system.

In addition, our device performance was compared with quantitative reverse transcriptase polymerase chain reaction (qRT-PCR) method (refer to supporting information S.6 and Fig. S8). As illustrated, the qRT-PCR method could provide a linear range from 5 fM to 50 nM and the LOD of 2.67 fM. In comparison with our device, qRT-PCR offered lower sensitivity and it was incapable of multiplex target detection in a single mixture. Also, qRT-PCR requires multiple enzymes and nucleotides as well as temperature cycling to make it complicated and costly.

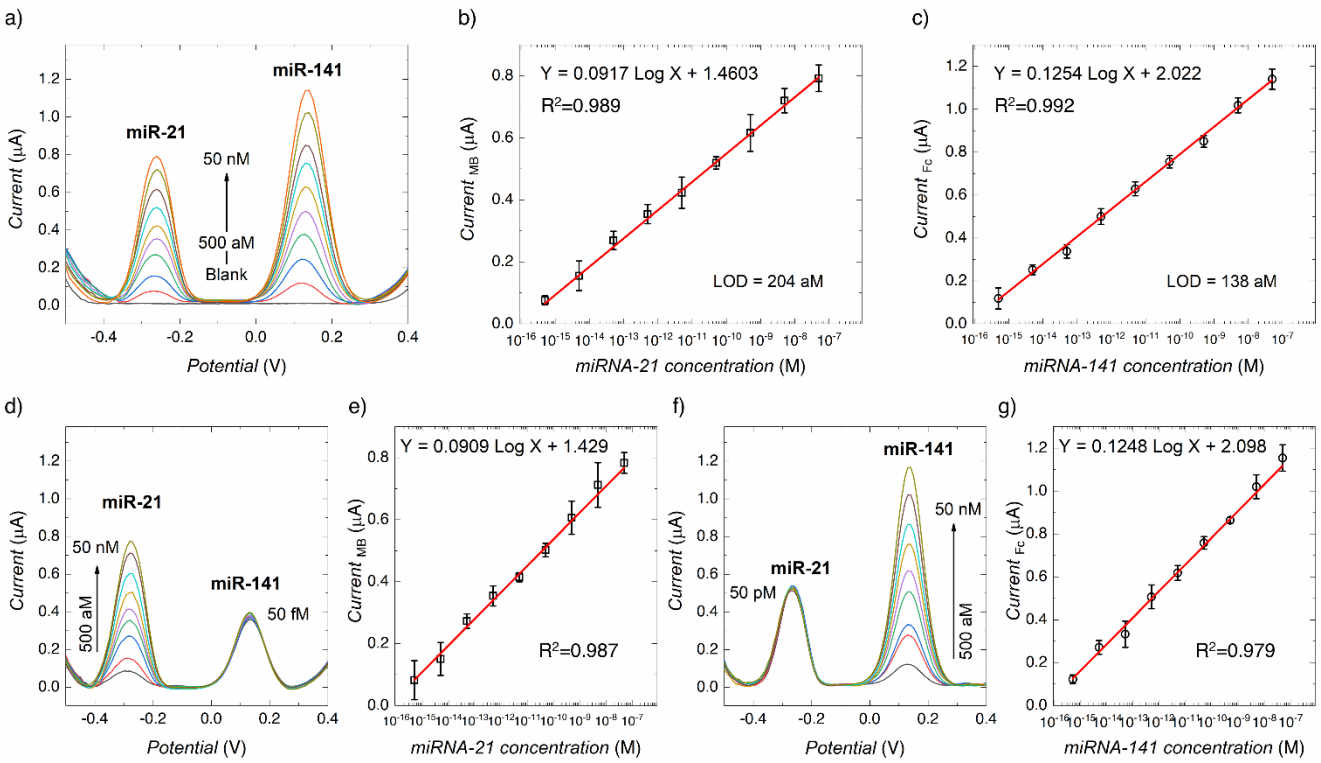

Figure 4. a) Typical DPV response of the fabricated biosensor device toward multiple detection of serial concentrations of miR-21 and miR-141 (0, 500 aM. 5 fM, 50 fM, 500 fM, 5 pM, 50 pM, 500 pM, 5 nM and 50 nM) in HEPES buffer (pH 7.4). b) and c) Corresponding regression plot illustrating the oxidation current peak values of MB and Fc as a function of miR-21 and miR-141 concentrations, respectively. d) Representative DPV response of the fabricated biosensor device toward single target detection of serial concentrations of miR-21 and constant value of miR-141 (50 fM). e) Plotting the MB oxidation current peak values as a function of miR-21 concentration. f) Typical DPV response of the fabricated biosensor device toward single target detection of serial concentrations of miR-141 and constant value of miR-21 (50 pM). e) Plotting the Fc oxidation current peak values as a function of miR-141 concentration. Statistical data was attained from eight different samples under equal conditions. The DPV curves are shown after baseline subtraction.

3.4. Evaluation of the biosensor performance

Due to the high specificity and selectivity of DSN to discriminate between the mismatched and perfectly-matched RNA:DNA heteroduplexes and also owing to the two step detection mechanism of our developed system, we envisaged to have a greatly selective and specific device. Selectivity of the fabricated biosensor was evaluated by cross-testing of the two sensing platforms. Three solutions containing (1) 500 pM miR-21 dissolved in a mixture of different miRNAs (miR-

155 and miR-152), (2) 500 pM of miR-141 dissolved in miRNA mixture, and (3) 5 pM of both miR-141 and miR-21 dissolved in miRNA mixture were prepared and subjected to the sensing assay. As depicted in Fig. 5a and the statistical plot of Fig. 5b, the biosensor showed a very selective response toward the target miRNAs. For the first mixture, an intense oxidation current peak arising from MB was seen which was almost identical to the peak value recorded for 500 miR-21 in Tris buffer (Fig. 4), whereas a very small peak for Fc was seen. Likewise, for the second mixture, the MB oxidation current peak was negligible while the oxidation current peak of Fc was significant and nearly equivalent to the value recorded for 500 pM miR-141 in Tris buffer. The biosensor response to the third mixture was also reasonably comparable to its response to the 5 pM miRNAs in buffer to demonstrate the high degree of selectivity of our developed sensing device.

In addition, the specificity test was conducted by analyzing the biosensor response to single-mismatched target miRNAs as well as non-complementary miRNAs. As it is clear in Fig. 5a and b, compared to the recorded signals for the complementary miRNAs (5 pM) there were 63.8% and a 68.5% damps in the observed signals for mismatched miR-21 and miR-141, respectively. This might be due to the fact that, mutation would slow down the DSN activity, also, it might result in a partial digestion of DNA sequences following by the production of long uncleaved DNAs to prolong their hybridization with sensing platforms due to the hysteresis effect (Gebala et al. 2013). Furthermore, very negligible responses were seen for the non-complementary miR-155 and miR-152 to prove the substantial specificity of the fabricate biosensor. Stability, reproducibility and repeatability analysis can be found in supporting information section S.7, Fig. S9 and Fig. S10.

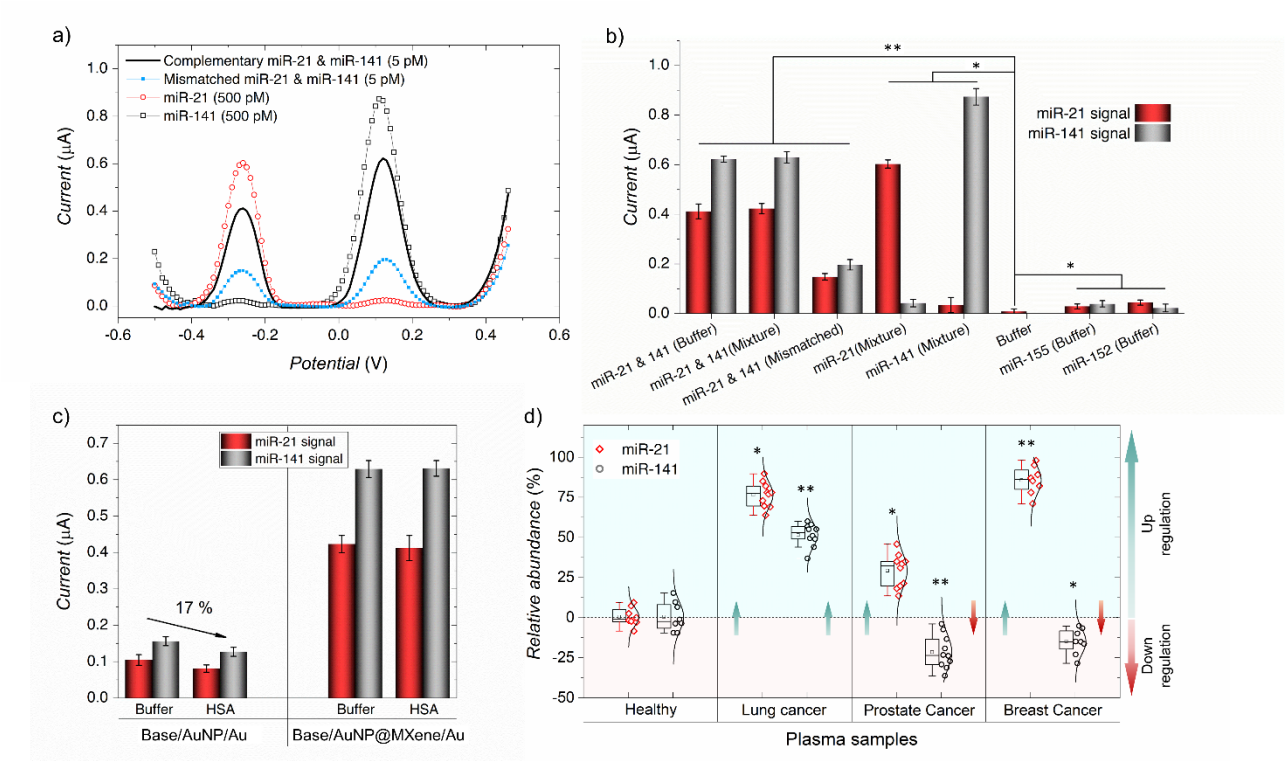

Figure 5. a) Comparison between DPV curves obtained from 5 pM target miR-21 and miR-141, 5 pM single mismatched miR-21 and miR-141, only miR-21 (500 pM) and only miR-141 (500 pM); Different concentrations were used to have more discrete and comparable curves. b) Statistical data obtained for the recorded oxidation current peak values arose from MB and Fc when introducing different analytes of: (from left to right) 5 pM miR-21 and miR-141 dissolved in Tris buffer and in a mixture of other miRNAs (miR-155 and miR-152), 5 pM mismatched miR-21 and miR-141, 500 pM miR-21 in a miRNA mixture, 500 pM miR-141 in a miRNA mixture, Tris buffer only, non-target miR-155 and miR-152; Depicted error bars were achieved based on analysis of 8 identical samples; $*P < 0.03$ and $**P < 0.05$ vs. control. c) Plotting the recorded signals on Base/AuNP/Au and Base/AuNP@MXene/Au for the detection of 5 pM miR-21 and miR-141 dissolved in Tris buffer and 10% HSA; Data was averaged based on three different identical experiments. d) Relative abundance of miR-21 and miR-141 in different plasma samples; Data was normalized against the healthy samples and stated as the standard deviation of mean value (n = 8) with normal distribution curves; $*P < 0.05$ and $**P < 0.04$ vs. corresponding healthy samples by ANOVA.

3.5. Real sample analysis

3.5.1. Antifouling properties of the modified electrodes

As mentioned earlier in the introduction part, MXene is known to possess the ability of resisting against the biofouling and non-specific bindings, therefore we expected that our device

would have a proper performance in real samples. A DSN amplification assay was lodged for 5 pM miR-21 and miR-141 spiked in 10% HSA. The resulting product was immobilized on two sets of electrodes comprising (1) Base/AuNP/Au and (2) Base/AuNP@MXene/Au. Notably, in all of the experiments for miRNA quantification in serum we used CHAPS at the optimized concentration of 10 μM, as we had already proved its role on minimization of interferences (Mohammadniaei et al. 2019a).

As seen in Fig. 5c, the signals recorded for Base/AuNP@MXene/Au for the detection of 5 pM miR-21 and miR-141 in 10% serum and Tris buffer were almost identical, whereas, Base/AuNP/Au represented around 17% lower signals for miRNAs in serum than that of the buffer. This might be due to the nonspecific bindings on the electrode surface to hamper the DNA:DNA hybridization efficiency. Therefore, MXene not only functioned as the electrochemical signal booster but also as the antifouling mediator to give rise to the reliability of our design. We also used different concentrations of spike-in miR-21 and miR-141 to verify sample recovery efficiency of the fabricated biosensor. As presented in Table S3, a sound recovery of 96.9% to 104.3% was seen demonstrating that the developed device has a significant potential to work in real biological samples.

3.5.2. Quantification of endogenous miR-21 and miR-141 in total human plasma

We investigated the validity of our fabricated device to quantify endogenous circulating miRNAs in total human plasma obtained from cancer patients and healthy donors (Table S4). The expression level of miR-21 and miR-141 in four different plasma samples of healthy, lung cancer (LC), prostate cancer (PC) and breast cancer (BC) were statistically analyzed and the obtained data points were normalized against the healthy samples. As seen in Fig. 5d, compared to the healthy

samples, miR-21 was up-regulated in all of the three cancer samples, as the highest value was allocated to the BC followed by LC and later PC samples. On the other hand, miR-141 was seen to be over-expressed in only LC samples, while lower-expressed in both PC and BC samples. Interestingly, the obtained data was fairly in consistence with the reported literatures for miR-21 and miR-141 expression levels in LC, PC and BC samples to prove the credibility of our device. Therfore, from the achieved data, the one can profile different types of cancers based on their unique miR-21 and miR-141 expression levels.

4. Conclusion

For the first time, AuNP-decorated MXene-$Ti_3C_2T_x$ as the electrochemical signal amplifier was coupled with DSN-based amplification on a SPGE electrode for a very specific, sensitive and rapid detection of multiple miRNAs in total plasma. The home-made SPGE electrode was designed for controllable and equal co-modification of $Base^{21\ \&\ 141}$/AuNP@MXene. Presence of MXene could elevate the electrochemical signal of the electrodes by almost 4 folds of magnitude, which was proved to be resulted from its vast surface area and high charge mobility. The 5 nm AuNPs were well- distributed within and on the MXene layers to amplify the electrochemical performance of MXene and supply the Thiol-Au bonding feature. The synergic effect of combining MXene-based electrochemical amplification and DSN target recycling, resulted in a (i) low assay time of 80 min, (ii) remarkable sensitivity of 204 aM and 138 aM for miR-21 and miR-141, (iii) high specificity (single-mutation recognition) and (iv) sound biofouling resistivity of the fabricated device. Due to the probe design simplicity and the considerable performance of the developed assay to profile three cancer plasmas, the fabricated 96-well adaptive sensing device can be upgraded for quantification of more analytes to become a prosperous device for POC cancer screening.

Acknowledgements

This work is supported by the Ministry of Trade, Industry, and Economy (Grant no. P000540 and Grant no. 20000580).

Appendix A. Supporting information

Supplementary data associated with this article can be found in the online version at doi:XXX

5. References

Abd-El-Fattah, A.A., Sadik, N.A.H., Shaker, O.G., Aboulftouh, M.L., 2013. Cell Biochem. Biophys. 67, 875–884.

Azzouzi, S., Fredj, Z., Turner, A.P.F., Ali, M.B., Mak, W.C., 2019. ACS Sensors 4, 326-334.

Chen, Y.-X., Huang, K.-J., He, L.-L., Wang, Y.-H., 2018a. Biosens. Bioelectron. 100, 274-281.

Condrat, C.E., Thompson, D.C., Barbu, M.G., Bugnar, O.L., Boboc, A., Cretoiu, D., Suciu, N., Cretoiu, S.M., Voinea, S.C., 2020. Cells 9, 276.

Feng, X., Gan, N., Zhang, H., Li, T., Cao, Y., Hu, F., Jiang, Q., 2016. Biosens. Bioelectron. 75, 308-314.

Gebala, M., La Mantia, F., Schuhmann, W., 2013. ChemPhysChem 14, 2208-2216.

Guo, L., Wang, J., Yang, P., Lu, Q., Zhang, T., Yang, Y., 2015. IUBMB Life 67, 720–725.

Guo, W.-J., Wu, Z., Yang, X.-Y., Pang, D.-W., Zhang, Z.-L., 2019. Biosens. Bioelectron. 131, 267–273.

Kilic, T., Erdem, A., Ozsoz, M., Carrara, S., 2018. Biosens. Bioelectron. 99, 525-546.

Kumar, S., Lei, Y., Alshareef, N.H., Quevedo-Lopez, M.A., Salama, K.N., 2018. Biosens. Bioelectron. 121, 243-249.

Lee, T., Mohammadniaei, M., Zhang, H., Yoon, J., Choi, H.K., Guo, S., Guo, P., Choi, J.-W., 2020. Adv. Sci. 7, 1902477.

Li, K., Jiao, T., Xing, R., Zou, G., Zhou, J., Zhang, L., Peng, Q., 2018. Sci. China Mater. 61, 728-736.

Li, P., Xu, T., Zhou, X., Liao, L., Pang, G., Luo, W., Han, L., Zhang, J., Luo, X., Xie, X., Zhu, K., 2017. Cancer Med. 6, 662–672.

Liu, C., Liu, R., Zhang, D., Deng, Q., Liu, B., Chao, H.-P., Rycaj, K., Takata, Y., Lin, K., Lu, Y., Zhong, Y., Krolewski, J., Shen, J., Tang, D.G., 2017. Nat. Commun. 8, 14270.

Liu, J., Jiang, X., Zhang, R., Zhang, Y., Wu, L., Lu, W., Li, J., Li, Y., Zhang, H., 2019. Adv. Funct. Mater. 29, 1807326.

Lorencova, L., Bertok, T., Dosekova, E., Holazova, A., Paprckova, D., Vikartovska, A., Sasinkova, V., Filip, J., Kasak, P., Jerigova, M., Velic, D., Mahmoud, K.A., Tkac, J., 2017. Electrochim. Acta 235, 471-479.

Lu, J., Wang, J., Hu, X., Gyimah, E., Yakubu, S., Wang, K., Wu, X., Zhang, Z., 2019. Anal. Chem. 91, 7353-7359.

Maduraiveeran, G., Sasidharan, M., Ganesan, V., 2018. Biosens. Bioelectron. 103, 113-129.

Mishra, S., Lin, C.-L., Huang, T.H.-M., Bouamar, H., Sun, L.-Z., 2014. Mol. Cancer 13, 212.

Mohammadi, H., Amine, A., 2018. Anal. Lett. 51, 411–423.

Mohammadniaei, M., Go, A., Chavan, S.G., Koyappayil, A., Kim, S.-E., Yoo, H.J., Min, J., Lee, M.-H., 2019a. Biosens. Bioelectron. 141, 111468.

Mohammadniaei, M., Lee, T., Yoon, J., Lee, D., Choi, J.-W., 2017. Biosens. Bioelectron. 98, 292-298.

Mohammadniaei, M., Nguyen, H.V., Tieu, M.V., Lee, M.-H., 2019b. Micromachines 10, 662.

Mohammadniaei, M., Yoon, J., Choi, H.K., Placide, V., Bharate, B.G., Lee, T., Choi, J.-W., 2019c. ACS Appl. Mater. Interfaces 11, 8779-8788.

Rakhi, R.B., Nayak, P., Xia, C., Alshareef, H.N., 2016. Sci. Rep. 6, 36422.

Song, B., Wang, C., Liu, J., Wang, X., Lv, L., Wei, L., Xie, L., Zheng, Y., Song, X., 2010. J. Exp. Clin. Cancer Res. 29, 29.

Steel, A.B., Herne, T.M., Tarlov, M.J., 1998. Anal. Chem. 70, 4670-4677.

Wang, J., Chen, J., Sen, S., 2016. J. Cell. Physiol. 231, 25–30.

Wang, M., Yin, H., Zhou, Y., Sui, C., Wang, Y., Meng, X., Waterhouse, G.I.N., Ai, S., 2019. Biosens. Bioelectron. 128, 137–143.

Wang, Y., Howes, P.D., Kim, E., Spicer, C.D., Thomas, M.R., Lin, Y., Crowder, S.W., Pence, I.J., Stevens, M.M., 2018. ACS Appl. Mater. Interfaces 10, 28290-28300.

Weber, J.A., Baxter, D.H., Zhang, S., Huang, D.Y., How Huang, K., Jen Lee, M., Galas, D.J., Wang, K., 2010. Clin. Chem. 56, 1733–1741.

Wu, L., Qu, X., 2015. Chem. Soc. Rev. 44, 2963-2997.

Xiao, Q., Li, J., Jin, X., Liu, Y., Huang, S., 2019. Sens. Actuators, B 297, 126740.

Zhang, X., Li, W., Zhou, Y., Chai, Y., Yuan, R., 2019. Biosens. Bioelectron. 135, 8–13.

Zhou, L., Wang, Y., Yang, C., Xu, H., Luo, J., Zhang, W., Tang, X., Yang, S., Fu, W., Chang, K., Chen, M., 2019. Biosens. Bioelectron. 126, 657–663.

Zhu, J., Ha, E., Zhao, G., Zhou, Y., Huang, D., Yue, G., Hu, L., Sun, N., Wang, Y., Lee, L.Y.S., Xu, C., Wong, K.-Y., Astruc, D., Zhao, P., 2017. Coord. Chem. Rev. 352, 306-327.

Zhu, W., Su, X., Gao, X., Dai, Z., Zou, X., 2014. Biosens. Bioelectron. 53, 414-419.